Handling of Propeller-Driven Propulsion System in High-Fidelity Aerodynamic Shape Optimization of Aircraft

Vicente Lhansol Massapina Vaz
vicentemassapinavaz70@tecnico.ulisboa.pt

Instituto Superior Técnico, Universidade de Lisboa, Portugal

November 2025

Abstract

Propeller effects cause significant changes in the wing's performance in tractor aircraft, and their understanding allows for design changes to improve performance. Propulsion models are used to estimate propeller effects in numerical simulations, with the actuator disk model being commonly adopted due to its simplicity, medium computational cost, and accurate time-averaged results. In this work, we study the actuator disk model and apply it to a case inspired by the TEKEVER AR5 drone. To complete the propulsion system, a nacelle geometry is introduced. A review of the propeller effects is documented, and the limitations of this propulsion model are explored. Since previous research using this model embedded in high-fidelity computational fluid dynamics found negligible improvements in unmanned aerial vehicle wing aerodynamic shape optimization, we revisit the same premise while focusing on the nacelle region. The nacelle and wing shapes are modified using the free-form deformation method, which includes a volume constraint to ensure sufficient space for the engine inside the nacelle. In our context, a two-step approach proved beneficial: first, optimizing the nacelle shape alone to improve design freedom, and then optimizing the wing and nacelle configuration. In our test case, this approach yields a 5% drag reduction compared to the case optimized without the actuator disk.

Keywords: Gradient-based optimization, adjoint method, free-form deformation, actuator disk, volume constraint, wing and nacelle configuration

1. Introduction

With the recent interest in hybrid and electric aircraft in today's highly competitive and ever-growing market of unmanned aerial vehicles (UAVs), the demand for improved designs of propeller-driven aircraft has never been so high. When developing new aircraft of the aforementioned type, the positioning and characteristics of the propulsion systems can improve the overall aerodynamic efficiency of the design.

The main objective will be to accomplish a series of aerodynamic shape optimizations of the propulsion model mounted on the wing of the AR5. While completing this objective, we also performed aerodynamic analysis with high-fidelity numerical tools, set up high-performance computing (HPC), created a propulsion model to carry out a study of a simple actuator disk model to estimate the wake and loads for propeller-driven aircraft, demonstrated its effects on a simple engine on-wing case based on the TEKEVER AR5 and how these effects are linked to propeller placement, and how the propeller affects aerodynamic shape optimizations.

The propulsion system will be comprised of the nacelle, modeled and mounted on the wing, along with the actuator disk model of the propeller, effectively capturing the aerodynamics of the full configuration of a wing. Furthermore, a surface constraint will be implemented, acting as a custom volume constraint inside the nacelle, whose shape will resemble the AR5's piston engine. This work is a follow-up of other theses related to TEKEVER, associated with the aerodynamic shape optimization of a wing [1], and aerodynamic shape optimization of a fuselage while considering volume constraints [2].

2. Aerodynamic Analysis

Computational fluid dynamics in aerodynamic optimization is typically performed by solving the Reynolds-Averaged Navier-Stokes (RANS) equations coupled with turbulence models [3]. This section provides the flow simulation parameters used in the aerodynamic analysis performed in this work.

2.1. Flow Simulation

For both the baseline isolated wing aerodynamic analysis and the mounted-wing aerodynamic analysis in this study, the cruise conditions of the TEKEVER AR5 were considered. Table 1 includes relevant performance parameters of the AR5 that were provided by TEKEVER for a previous study [1].

Table 1: Parameters of the TEKEVER AR5.

Cruise speed	U_∞	100	km/h
Cruise altitude	h	305	m
Reference chord	c	0.6091	m
Reference area	S	2.1691	m^2
Wing lift coefficient	C_{L_wing}	0.8932	

All the aerodynamic analyses were performed with ADflow [3], and more specifically, using the *AeroProblem* Python function. Some input values are required, such as altitude, reference area, reference chord, angle of attack, and Mach number. A few parameters were already given in Table 1. The Mach number, was set to $M = 0.08164$, the Reynolds number, was set to $Re \approx 1.1 \times 10^6$ and an angle of attack of $\alpha_\text{cruise} = 1.9°$, since this achieved the required C_{L_wing} for cruise conditions [1].

The CFD simulations solved the steady RANS equations, coupled with the Spalart-Allmaras (SA) turbulence model [4]. Some solver values provided in [1] were altered: `L2Convergence` was considered to be 10^{-8}, and `anksecondordswitchtol` to be 10^{-4}. Regarding discretization, central difference with JST scalar dissipation was used, and other parameters were kept at the default values as determined by Gameiro [1]. For the NK solver, a GMRES subspace of dimension 60 was employed to solve the linear systems. The Eisenstat-Walker algorithm was utilized to control linear convergence at each iteration. An additive Schwarz method served as the global preconditioner for the NK, ANK, and adjoint solvers. The Jacobian matrix used in the preconditioner is lagged by 20 iterations in the NK solver and by 10 iterations in the ANK solver, by default [1, 5].

All simulations were performed on an HPC machine with 128 GB of memory and an AMD® Ryzen 9 7950x 16-core processor.

3. Propulsion Model

The actuator disk model represents the propeller mounted on this work's wing. The model simplifies the propeller's geometry to a distribution of time-averaged forces over a disk using source terms or boundary conditions [6]. The propeller forces consist of two types: axial and tangential forces. A typical, simple method for modeling the distributions of axial and tangential loading on the propeller was developed by Hoekstra [7]. The radial distribution for the axial force is given by

$$f_x(r) = \hat{F}\hat{r}^m \left(\frac{a-\hat{r}}{a}\right)^n \quad , \tag{1}$$

where the parameters a, m, and n, which determine the shape of the force distribution, f_x is the axial force per unit radius, $\hat{F}$ is a reference value adjusted to obtain the required total force, and $\hat{r}$ is defined as

$$\hat{r} = \frac{r - r_\text{in}}{R - r_\text{in}} \quad , \tag{2}$$

where r is the radial distance from the axis of rotation, r_in is the spinner radius of the propeller and R is the outer radius of the propeller. In our work, the radial distribution for the tangential forces is different from the version used by Chauhan et al. [6, 8], and it was given by

$$f_{\phi_\text{new}}(r) = \hat{F}'\hat{r}^m \left(\frac{a-\hat{r}}{a}\right)^n \quad , \tag{3}$$

where f_{ϕ_new} is the tangential force per unit radius (its sign will dictate the rotation direction of the rotor), and $\hat{F}'$ is another reference force adjusted to obtain the total torque. This modification was provided by Matos (private communication, Dec. 2024). By considering that the propeller is made of an infinite number of blades, both forces will depend only on the radial position. As such, the rotational speed, azimuthal position, and number of blades are no longer required. For simulations with different rotational speed using the actuator disk model, one would simply have to recalibrate the total thrust and torque to obtain consistent values.

3.1. Propeller Inputs

This propeller model is defined to emulate the forces generated by the TEKEVER AR5's propeller, by using Eq.(1) and Eq.(3) and creating the resulting distribution plotted in Fig.1, which is then rotated asymmetrically across the given axis of thrust direction.

Similarly to the real AR5 propeller, the generated disk has a radius of 0.3874 m, and a spinner radius of 0.05 m. In this study, the distribution parameters for Eqs.(1) and (3) were $a = 1$, $m = 1$, since this is an open duct propeller, as suggested in [7], and $n = 0.5$. The pitch-to-diameter ratio is not considered because it is not required to model the used tangential force distribution in Eq. (3), and the total torque generated is a known value. Additionally, due to the chosen orientation of the mesh of the wing, this work assumes that a positive f_ϕ will result in a rotation direction of inboard up (IU). The inputs for total propeller thrust and torque are 109.26 N and 8.70 N · m, respectively.

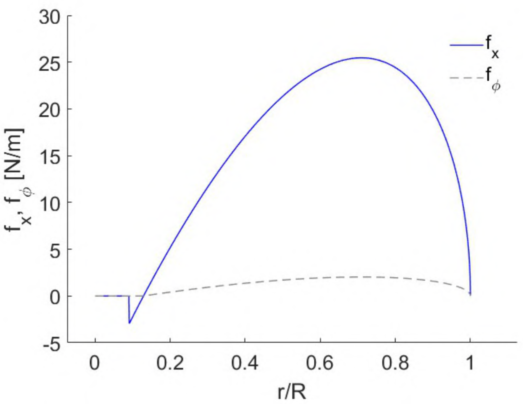

Figure 1: Propeller axial and tangential forces distribution.

3.2. Model Shortcomings

Since this consists of an axisymmetric propeller model, it will fail to account for the asymmetric loading that arises at non-zero angles of attack. In reality, the angle of attack introduces variations in the flow conditions experienced by each blade; the up-going blade encounters a lower effective angle of attack and reduced relative velocity (since a small blade velocity component is aligned with the freestream velocity). In contrast, the down-going blade faces higher values of both. This asymmetry leads to the up-going blade generating less axial and tangential force, and the down-going blade generating more at positive angles of attack [6].

Additionally, while in [6] it was determined through comparison with experimental values that an actuator disk with a zero angle of attack provided correct results for the wing loading, [9] also notes that the wing-induced vertical upwash can also effectively increase the propeller's angle of attack. However, this effect is diminished if the tractor propeller is not closely coupled to the wing (as in our case), and [6] also considers a single-interaction-mode (SIM) propulsion model, so the wing-induced upwash acting on the actuator disk was ignored.

Nevertheless, the actuator disk model was deemed a viable option, as the results are similar to experimental data [6]. We do note, however, that to achieve results with acceptable accuracy, the angle of attack of the configuration should be as close to 0° as possible.

3.3. Impact of Propeller on the Wing

The most recognizable wing-propeller interaction effects are evidenced in wing loading distributions [10]. Figure 2 presents the lift distribution from the ADflow simulation coupled with the actuator disk for the AR5 case.

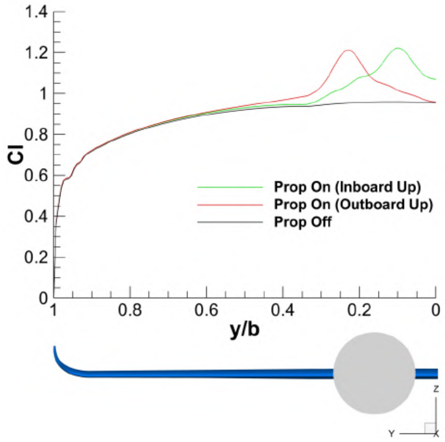

Figure 2: Simulated wing lift distribution results for different propeller rotation directions.

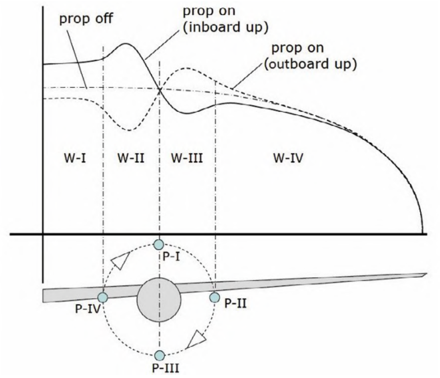

Figure 3: Influence regions due to propeller wing interaction on loading distribution [11].

The regions defined by Veldhuis [11] are divided into different regions of influence of propeller slipstream, which cause a very significant change in the wing's performance, especially in regions W-II and W-III, which are directly behind the propeller. Focusing on the inboard up distribution in Fig.3, the region W-II of the wing receives the propeller upwash and, as a result, it has increased dynamic pressure and the upward velocity increases the local angle of attack, which enhances the lift on that section of the wing [6, 9]. In the region W-III, the wing receives the slipstream of the propeller downwash, causing the opposite, thus the lift on the wing is locally decreased. The remaining regions W-I and W-IV are also changed due to the propeller altering the wing inflow conditions and disturbing the vorticity sheet leaving the wing [11].

We can see that the TEKEVER AR5 wing, coupled with the actuator disk in Fig.2, has a slightly dissimilar loading distribution to the theoretical wing and that of similar studies [6]. Namely, the downwash region in both rotation directions does not have a lower lift when compared to the isolated wing, and for the inboard up rotation direction, the region W-IV of the AR5 wing is practically unaltered. The downwash effect produced by the actuator disk torque is much less accentuated than the upwash effect, and the supposedly neutral spinner zone, where the lift of all configurations should be the same, does not match.

The AR5 wing airfoil exhibits greater camber than other wings with a loading distribution closer to the one in Fig.3, such as the wing used in [6] for the validation cases, which uses the NACA 64_2-A015, which is a symmetric airfoil. The greater curvature of the mean camber line might have the same effect as inclining the propeller angle of attack downwards, which raises the section lift in the spinner zone, as also seen in [12].

Additionally, the AR5 propeller is small when compared to other examples, and has lower disk loading since it belongs to a UAV. Stronger propellers with higher disk solidity will also cause more noticeable distortions to the inflow of the wing. The low torque used to simulate the actual AR5 propeller causes a weaker downwash, which is further countered by the higher local lift caused by the propeller-induced axial velocity.

There is also an increment in lift in the propeller spinner zone, unlike in the Fig.3, which can be attributed to the propeller pitch angle [12]. Since no propeller pitch was used, the occurrence of this offset ties into the reason that the camber of the airfoil could be causing this effect. Besides this, the increase in lift in this region explains the increase in the total wing C_L, and due to the effective angle of attack increasing, so will the pressure drag in this region, which explains the increase in total wing C_D. Another note is that the ratio between the latter two parameters is higher in the inboard up case than in the outboard up (OU) case, as theory tends to suggest [13].

3.4. Impact of the Nacelle on the Wing

Before discussing the impact of the nacelle on the wing's performance, we must acknowledge the limitations of our simulation models. It has been shown that a wing and nacelle configuration with an axisymmetric actuator disk will bear accuracy errors for the time-averaged solution [14], since the propeller model does not account for airframe interference or the aforementioned blade angle of attack variations for non-zero angles of attack [14]. Ignoring the effects of the wing on the propeller is acceptable on a tractor configuration if the wing is sufficiently far away from the propeller [9], but the same cannot be assumed when a nacelle is closely behind the propeller. Its proximity will have a considerable effect on the inflow of the propeller, thus changing its thrust and power distribution. Despite the errors of the axisymmetric disk, the estimated performance of the configuration and force distribution of the propeller forces will be similar to that of the "enhanced disk" in [14], and a passable solution can be obtained with our original actuator disk.

In our meshing process, the nacelle mesh was joined to the AR5 wing using the half-collar method, which facilitated the implicit hole cutting (IHC) process by reducing the number of overset blocks. Other studies have dealt with the aerodynamic effects of a nacelle on a propeller-wing regarding a larger turboprop transport airplane [15], and a smaller configuration closer to the AR5 size [9]. In [9], it is stated that the presence of a nacelle similar to this one causes a small axial velocity increase in some regions of the propeller. In [15], the study discloses four unfavorable effects caused by the engine nacelle on the aerodynamic performance of the wing for high-lift configuration (high angle of attack and flap deflection), which, when combined, exacerbate the adverse pressure gradients between the wing's leading edge and the high-pressure flow expand border on the upper surface of the main wing behind the nacelle, thus accelerating flow separation in this region. This will result in worse aerodynamic performance compared with the clean wing configuration, and the occurrence of stall will be expedited. To mitigate this issue, the authors suggested reducing the height of the installation of the nacelle on the wing or modifying the geometry of the junction zone, which solved the problem of increased drag while delivering good performance during high-lift configurations.

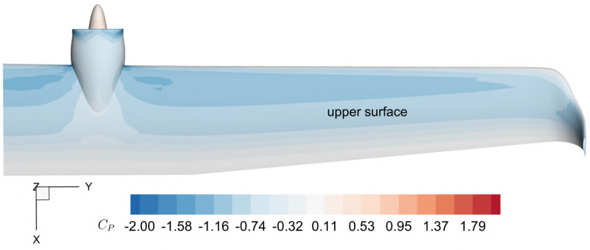

Figure 4: TEKEVER AR5 cruise configuration.

Despite some differences in the turbulence model and flow conditions employed in [15], we might conclude that the AR5 also experiences the higher-pressure flow expansion effect on the upper surface of the main wing, albeit with much weaker adverse pressure gradients in cruise conditions, as seen in Fig.4. This effect will cause the leading edge of the nacelle and its surrounding region to be more prone to flow separation. Considering also the blunt geometry of the nacelle's front, we can expect that this zone will have separated flow for the majority of flight conditions. Additionally, at larger angles of attack, the strength in these adverse pressure gradients will also increase, causing high lift losses sooner when compared with the clean AR5 wing.

The increased circulation intensifies spanwise pressure gradients, causing stall to occur earlier in the suction side of the nacelle region than it would for a clean wing.

To see how these effects intertwine with the propeller, we can also add the actuator disk to the simulations which include the nacelle. The biggest impact results from the vorticity inserted by the actuator disk, which now interacts with both the wing and the nacelle. Figure 5a presents the streamlines passing through the actuator disk, on the nacelle region, with an inboard-up rotation direction at cruise conditions. The pressure distribution on the surface of the wing and nacelle was also plotted.

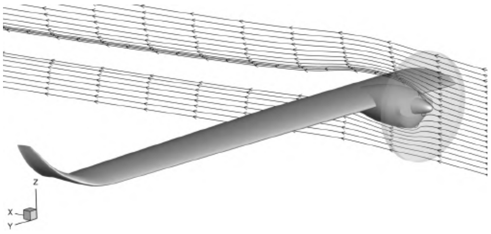

(a) Full configuration.

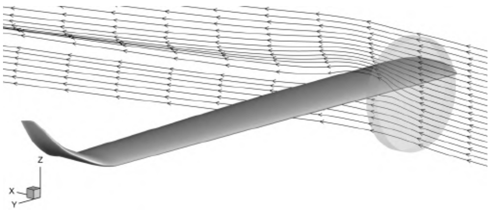

(b) Wing and propeller configuration.

Figure 5: Deflected streamlines.

We can see that right after the actuator disk, all streamlines are immediately affected by the nacelle. The streamlines passing near the spinner region of the actuator disk (vortex core) exhibit swirl downstream of the wing. The streamlines below the spinner show a shift toward the root of the wing, and those above shift toward the tip, as they are rotating in accordance with the disk's inboard up rotation. The flow in Fig.5a does not attach to most of the suction side of the wing, signifying possible separation in this region, contrary to what is shown in Fig.5b. The early separation in the nacelle region will create a larger wake, thus an increase in pressure drag, C_{D_p}, is expected.

Table 2: Impact of the nacelle on aerodynamic performance.

Nacelle	Propeller	C_L	C_{D_p}	C_{D_f}
Yes	Yes	0.9179	0.0369	0.0102
Yes	No	0.8793	0.0330	0.0097
No	Yes	0.9501	0.0304	0.0106
No	No	0.8945	0.0255	0.0098

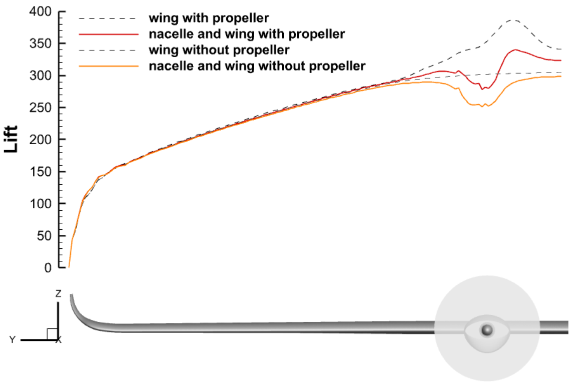

Figure 6: Effect of the nacelle on the wing lift distribution.

We confirm this comprehensively from the results obtained for all possible configurations in Tab.2. The presence of the nacelle causes a lift loss, and the increase in C_{D_p} is verified (of 38% for the case including the propeller, and 35% without it). Intuitively, the wing with the nacelle has a larger wetted area at the same flow conditions and since the CFD data is nondimensionalized using the same reference area, they should exhibit higher C_{D_f}. However, the nacelle region is more susceptible to separation and, in this case, the balance between the extra surface area with separated flow and turbulent flow causes the total C_{D_f} to remain approximately the same when compared to the clean wing configuration.

To visualize how the nacelle impacts the wing loading, all configurations are shown in Fig.6. Only the inboard up rotation direction was considered. The presence of the nacelle causes a very noticeable impact on the lift distribution, it occupies a small portion of the wing, but its presence disrupts one-third of the span of the flow around the wing, resulting in a $C_L = 0.8793$, which corresponds only to a loss of lift of -1.7% when compared with the isolated wing in cruise conditions, but a large increase in pressure drag of 22.7%. The effect of the disruption is a lift crater similar to that caused by the fuselage in [1], showing again another possible effect of flow separation in this region. However, the lift losses caused by the AR5's nacelle are not representative of the actual wing performance, since, as seen before, the actuator disk is responsible for increasing lift.

In conclusion, we find that the presence of the nacelle disrupts the typical flow characteristics of the isolated AR5 wing, reducing lift and increasing pressure drag due to flow separation and its aggravation. From [15], we also see that the slight changes to the positioning or the geometry of the nacelle in relation to the wing can deliver great improvements for its aerodynamic performance. Also, the negligible impact of the nacelle seen in studies with streamlined nacelles shows that it is possible for their geometry not to be so prejudicial in this aspect, especially for configurations in similar flight conditions to the AR5. For these reasons, it might be beneficial to include the nacelle while optimizing the wing. Despite the accuracy errors of the actuator disk force distribution, we will perform optimization shape of the nacelle while accounting for the propeller forces.

4. Shape Optimization Framework

The gradient-based Sequential Least Squares Quadratic Programming (SLSQP) algorithm [16] was chosen since it has been applied in previous aerodynamic shape optimization and is well-suited for solving constrained nonlinear optimization problems [1].

The sensitivity method used in ADflow is the adjoint method [17]. Since its computational cost does not depend upon the number of design variables, it is ideal for aerodynamic shape optimization problems, where the number of design variables is much larger than the number of functions of interest. The approach that ADflow uses to compute the terms necessary to form the discrete adjoint equations is automatic differentiation [3].

For the shape deformation technique, we will be using free-form deformation (FFD). Some studies have used the FFD method for configurations with multiple components using the MACH-Aero framework [18]. However, their implementations are complex, and the intersection cases differ from the intersection between the nacelle and wing of the AR5 configuration. As such, a simple approach for the FFD box strategy was considered, embedding the entire wing and nacelle configuration in a single volume. This approach reduced the parametrization quality in the intersection region between the nacelle and the leading edge of the wing, due to the way the surface mesh is projected into the FFD box, and limited the design freedom of the nacelle itself. Our solution to the latter was to perform the aerodynamic shape optimization in two steps: the initial one with just a separate nacelle, and then joining the result to the AR5 wing (recreating the half-collar mesh) for an optimization of the nacelle region on the wing.

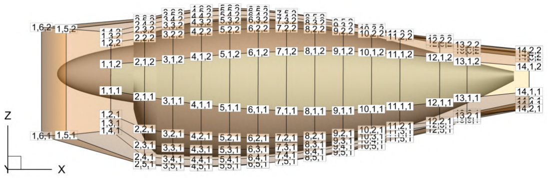

Figure 7: Side view of the FFD volume of the separated nacelle.

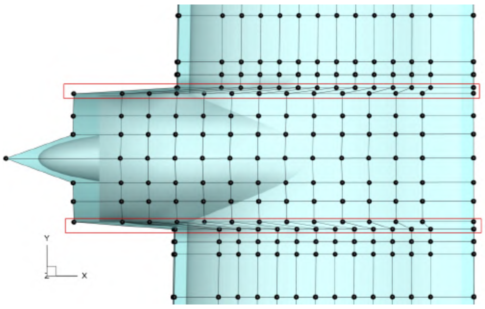

Figure 8: Adopted strategy for the following optimization problems.

Only less than half of the FFD points along the chordwise direction were selected to move, meaning only the sections of points $[1, y, z]$ until $[5, y, z]$ shown in Fig.7, since the latter points are supposed to be displaced in the subsequent optimization. The selected points do not include those encompassing the nacelle's spinner, in order to freeze its shape. After deforming the nacelle, we reinsert the nacelle's shape on the wing and create a fully embedding FFD volume. However, this still implies that the leading edge on the intersection region with the nacelle, one of the most important zones that would benefit from aerodynamic shape improvement (as discussed in Section 3.4), will be frozen during optimization, which poses a substantial limitation for the fully embedding FFD volume. This region is delineated in red in Fig.8, which shows the chosen FFD solution for the optimizations. The zone being optimized will consist only of the region between these two sections, the nacelle region.

The chosen design variables are the local shape variables, as will be defined in Tab.4, which allow for small shape modifications by moving the FFD point along one defined axis. They are utilized for airfoil optimization [1] and fuselage optimization [2], therefore being the most appropriate for the nacelle region.

The geometric constraints consist of thickness constraints, volume and triangulated surface constraints, and leading-edge and trailing-edge constraints. The triangulated surface constraint is the most complex implementation, explored extensively in [2]. It requires using other software or other libraries, such as PyVista, to create the triangulated surface of the part, so that during the optimization process, the intersections between the part and the shape being optimized can be computed. We will use this method to represent the geometry of the engine of the AR5 in a simplistic but efficient manner, as seen in Fig.9.

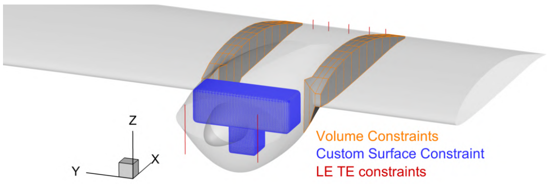

Figure 9: Geometric constraints applied to the AR5 wing and nacelle configuration.

5. Aerodynamic Shape Optimization

We will be performing several single-flight-point optimization problems. In this work, the objective will always be to minimize the drag coefficient. Additionally, we will determine whether the propeller effects are beneficial during an aerodynamic shape optimization process for a wing and nacelle configuration [6].

5.1. Optimization Problem Definition

To achieve this goal, we will have one case optimized without an actuator disk, and two others with it, one for each rotation direction. After obtaining the results, we include the actuator disk and perform a trim operation on the first case. This consists of an optimization with solely the angle of attack as a design variable [1], with the same $C_L = C_{L_{cruise}}$ constraint, allowing us to directly compare the case optimized without the propeller effects to the others. However, as seen previously, higher angles of attack have associated accuracy errors. Therefore, the actuator disk should be perpendicular to the freestream flow velocity direction, which means $\alpha_p = 0°$, for all cases. This poses a problem for our cases, since the angle of attack of the entire configuration is a design variable, which means altering the freestream flow direction, and thus α_p. The angle of attack of the optimized solutions can differ from one case to another, and as such, direct comparisons between them might be flawed. Previous studies [6] have resolved this issue by establishing every FFD section with twist variables, which effectively emulated the angle of attack design variable, and fixed the freestream velocity direction to have the previously stated $\alpha_p = 0°$. This method ensures that each case is subjected to the same propeller inflow, but the wing angle of attack of the baseline case can be freely altered to obtain the desired C_L. Nevertheless, this approach is incompatible with our optimization problems because our configuration includes a nacelle. In the latter study, the difference in relative angle between the wing and the propeller across the cases was regarded as an unaddressed design variable, and the consistency of propeller inflow was prioritized, but the presence of the nacelle requires that the spinner position and orientation remain fixed in relation to the actuator disk, disallowing this method. With no other option available for propeller effects prediction for our cases, we must assume this error. To mitigate this issue, we only study cruise conditions, where the angle of attack is relatively small, as the level flight optimization results showed.

In this work, the convergence accuracy of the SLSQP algorithm was set to 1×10^{-3}, several orders of tolerance above the adjoint tolerance, of 1×10^{-7}, since the adjoint solution is usually less accurate than the required optimality. The maximum number of iterations for the optimization algorithm was set to 500. The optimization problem of the separate nacelle case is presented in Tab.3.

Table 3: Formulation of the separated nacelle optimization problem.

	Function/Variable	Quantity
minimize	C_D	
w.r.t.	$-0.05 \leq \Delta y \leq 0.05$	90
	$-0.05 \leq \Delta z \leq 0.05$	70
	Total design variables	**160**
subject to	$KS_{geom} \leq 0$	1
	$L = 0$	1
	Total constraint functions	**2**

The constraints of spatial feasibility explicit in the last two rows of Tab.3 relate to the engine volume constraint, shown in blue in Fig.9. The points in rows $[x, 1, z]$ and $[x, 11, z]$ did not include a vertical displacement to avoid infeasibility, as the nacelle tended to become pinched in its sides. Flow conditions were those of the cruise flight, with a fixed angle of attack of 1.9°. The optimization problem will be repeated for each actuator disk configuration.

5.2. Optimization without the Propeller

After obtaining the optimized nacelle separately, we join it to the wing and perform an optimization of the nacelle's region on the wing according to the problem defined in Tab.4. The result of the case without propeller is presented in Fig.10. We can see that the optimized shape shrinks the nose of the nacelle, reducing the area perpendicular to the flow, making it more streamlined. This alleviates the strong adverse pressure gradient on the front of the baseline geometry, seen in Fig.4, which is complemented by the fact that the negative skin friction region in the nose from Fig.11 to Fig.10 has decreased substantially, likely meaning that flow separation has been reduced in this region.

Optimizing the nacelle separately at first was also beneficial, as the sides on the front were able to

Table 4: Formulation of the nacelle and wing optimization problem, including a triangulated surface constraint.

	Function/Variable	**Description**	**Quantity**
minimize	C_D	Drag coefficient	
w.r.t.	$0 \leq \alpha \leq 3$	Angle of attack of the entire configuration. [deg]	1
	$-0.05 \leq \Delta z \leq 0.05$	Vertical displacements of the FFD control points encompassing the nacelle sections. [m]	128
		Total design variables	**129**
subject to	$C_L = 0.8932$	Lift constraint	1
	$t/t_{\text{initial}} \geq 0.9$	Volume constraints to maintain acceptable airfoil and intersection thickness.	2
	$\Delta z_{\text{LE,upper}} = -\Delta z_{\text{LE,lower}}$	Constraints of the selected leading edge FFD control points to impede shear twist in the nacelle.	2
	$\Delta z_{\text{TE,upper}} = -\Delta z_{\text{TE,lower}}$	Same as the previous constraint, but applied on the trailing edge FFD control points in the nacelle sections.	5
	$KS_{geom} \leq 0$	Aggregated minimum distance (spatial feasibility Condition 1)	1
	$L = 0$	Non-intersection (spatial feasibility Condition 2)	1
		Total constraint functions	**12**

be narrowed, and inflating the midsection provided smoother area transitions, thereby ensuring less aggravated pressure gradients, which allowed for increased flow attachment. This idea is further evidenced by the values of pressure and viscous drag in each solution.

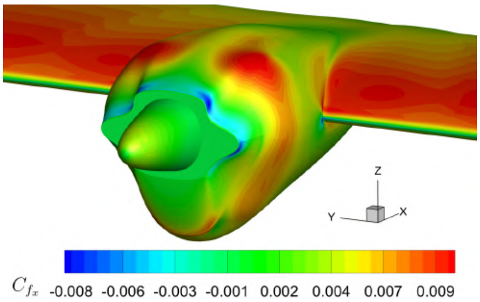

Figure 10: Optimized C_{f_x} distribution of the separated nacelle, without a propeller.

We see that the C_{f_x} distribution remained unchanged in the intersection of the nacelle and the wing's leading edge, likely because our parameterization in this zone is inadequate. As seen previously, the resulting circulation in this zone is also responsible for flow separation, and it could have been improved if the optimization had been performed with a strategy that accounted for component intersections [18].

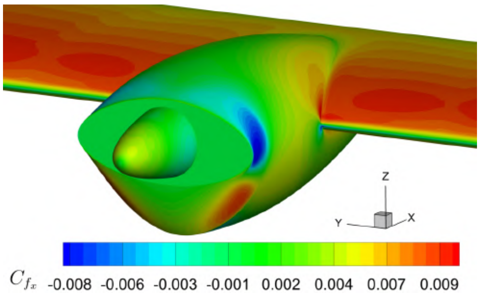

Figure 11: Baseline $C_{D_{f_x}}$ distribution without a propeller.

5.3. Optimization with the Propeller

The inboard up case's result is presented in Fig.12. The outboard up case resulted in a very similar but mirrored solution, so it will not be discussed here.

There are more differences in the cases which include the propeller. Most notably, the optimized shape is asymmetric, which might help improve the swirl recovery property of the wing, bringing the wing loading close to an optimal distribution, which is not necessarily elliptical, as stated in [13], due to the propeller's influence on the "clean wing" slipstream. We can visualize by plotting a slice of the non-dimensional spanwise velocity component, U_y, and noticing that the newer solution in Fig.13a has a reduced area with lower values of U_y that accompany the inboard up rotation of the disk, when compared with the baseline case in Fig.13b.

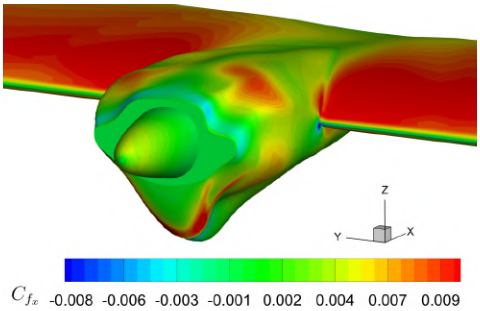

Figure 12: Optimized C_{f_x} distribution of the separated nacelle, with an IU propeller.

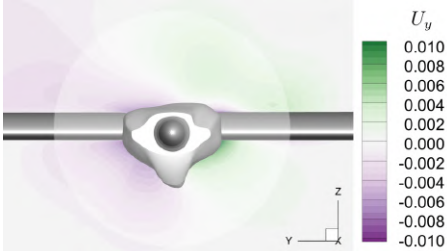

(a) Optimized nacelle.

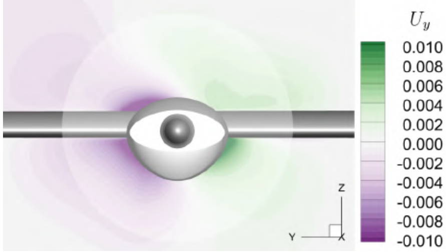

(b) Baseline nacelle.

Figure 13: Spanwise velocity component distributions, with an IU propeller.

The solutions also show reduced thickness in the region of the wing behind the nacelle. It seems to benefit from the reduced thickness to decrease induced drag by reducing the wake's width. The nose of the nacelle has also been improved similarly to the previous optimization case without the propeller, as we can see by analysing Fig.12.

5.4. Level flight Analysis Comparison

Lastly, we must add an actuator disk and perform a flight leveling operation on the solutions of the cases optimized without an actuator disk, so that all optimized solutions have the same $C_{L_{\text{wing}}}$ and are comparable. We can also assume there are similar propeller errors due to similar angles of attack, whose results ranged from 1.5° to 1.7°. The cases optimized with the actuator disk are already leveled according to the defined lift constraint. The results are shown in Tab.5, and the drag reductions are computed in relation to the baseline case with the corresponding propeller rotation direction.

Table 5: Level flight results for each case with the nacelle separately optimized first.

Optimized	Added AD	ΔC_D	ΔC_{M_y}
without AD	IU	-3.94%	-0.86%
with IU AD	-	-8.75%	$+0.91\%$
without AD	OU	-3.93%	-0.86%
with OU AD	-	-8.73%	$+0.47\%$

While stability studies of the aircraft were not considered in this work, the ΔC_{M_y} results in Tab.5 suggest small changes in relation to the leveled baseline value, indicating that these optimized shapes will not significantly affect the initial stability condition of the AR5.

In regards to ΔC_D results, we find that cases optimized while accounting for propeller forces improved significantly more in relation to cases optimized without them. With this parameterization method, we found that if the nacelle and wing were optimized with an actuator disk, the result would benefit from a 5% total drag reduction in relation to being optimized without it, for both rotation directions. If we ignore the accuracy errors described in previous sections, this is a much more satisfactory result than the negligible improvements found in [6]. However, the total time required for a complete optimization case without an actuator disk was 28 hours, with an inboard up propeller was 33 hours, and with an outboard up propeller it was 42 hours, due to the increased complexity of the flow in each aerodynamic analysis.

6. Conclusions

In this work, the MACH-Aero framework was used to perform several aerodynamic analyses and solve various aerodynamic shape optimization problems incorporating propeller and nacelle effects. By employing the actuator disk to model the propeller effects, we were able to provide accurate, time-averaged results using ADflow. To address issues related to the design freedom of the nacelle, the parameterization was rectified with the two-step optimization process. It was found with proper parametrization, including the actuator disk in the optimization of the nacelle region on the TEKEVER AR5 wing would reduce drag by 22 counts for both propeller rotation directions, using only shape deformation design variables, but requiring 5 more hours of total computational time to complete the case which included the inboard up propeller, and more 14 hours for the outboard up case. Nevertheless, performing the optimization while ignoring the propeller effects still provided good results, reducing total drag by 34 counts when compared to the baseline.

For future work, it is recommended to create a version of the modified actuator disk model in ADflow that uses the local angle of attack of the upstream cells near the actuator disk region to more accurately model the propeller at non-zero pitch angles, or when it is affected by the upwash of a wing or a nacelle. Finally, since the optimization results of our study showed good drag reductions of the isolated nacelle and wing while considering only the nacelle region of the wing, the next studies should implement a parametrization that takes component intersections into account, which would allow the wing to be separately optimized with global variables in conjunction with the added design freedom of the nacelle.

References

[1] R. da Silva Gameiro. Aerodynamic design of a MAME UAV wing using high-fidelity numerical tools. Master's thesis, Instituto Superior Técnico, Portugal, November 2023.

[2] L. Pinheiro. Aerodynamic shape optimization of UAV fuselage and fairings with payload integration. Master's thesis, Instituto Superior Técnico, Portugal, July 2025.

[3] C. A. Mader, G. K. W. Kenway, A. Yildirim, and J. R. R. A. Martins. ADflow: An open-source computational fluid dynamics solver for aerodynamic and multidisciplinary optimization. *Journal of Aerospace Information Systems*, 17(9):508–527, September 2020. doi: 10.2514/1.I010796.

[4] P. Spalart and S. Allmaras. A one-equation turbulence model for aerodynamic flows. *AIAA*, 439, January 1992. doi: 10.2514/6.1992-439.

[5] MDO Lab. MACH-Aero documentation, 2022. URL `https://mdolab-adflow.readthedocs-hosted.com/en/latest/solvers.html#interpreting-output`. ADflow Solvers.

[6] S. S. Chauhan and J. R. R. A. Martins. RANS-based aerodynamic shape optimization of a wing considering propeller-wing interaction. *Journal of Aircraft*, 58(3):497–513, May 2021. doi: 10.2514/1.C035991.

[7] M. Hoekstra. A RANS-based analysis tool for ducted propeller systems in open water condition. *International Shipbuilding Progress*, 53:205–227, January 2006. doi: 10.3233/SHP-2006-isp011.

[8] S. S. Chauhan and J. R. R. A. Martins. Rans-based aerodynamic shape optimization of a wing with a propeller in front of the wingtip. *Aerospace*, 11(7), 2024. doi: 10.3390/aerospace11070512.

[9] L. Veldhuis. Review of propeller-wing aerodynamic interference. ICAS 2004-6.3.1. In *24th International Congress of the Aeronautical Sciences, Yokohama, Japan*, 2004.

[10] C. Alba, A. Elham, B. J. German, and L. L. Veldhuis. A surrogate-based multi-disciplinary design optimization framework modeling wing–propeller interaction. *Aerospace Science and Technology*, 78:721–733, 2018. doi: 10.1016/j.ast.2018.05.002.

[11] L. Veldhuis. *Propeller Wing Aerodynamic Interference*. PhD thesis, TU Delft, June 2005. Netherlands.

[12] L. Veldhuis and P. Heyma. Aerodynamic optimisation of wings in multi-engined tractor propeller arrangements. *Aircraft Design*, 3(3): 129–149, 2000. doi: 10.1016/S1369-8869(00)00010-0.

[13] I. Kroo. Propeller-wing integration for minimum induced loss. *Journal of Aircraft*, 23(7): 561–565, 1986. doi: 10.2514/3.45344.

[14] A. Gomariz-Sancha, M. Maina, and A. J. Peace. Analysis of propeller-airframe interaction effects through a combined numerical simulation and wind-tunnel testing approach. In *53rd AIAA Aerospace Sciences Meeting*. AIAA, 2015. doi: 10.2514/6.2015-1026.

[15] Y. Qiu, J. Bai, and L. Qiao. Aerodynamic effects of wing-mounted engine nacelle on high-lift configuration of turboprop airliner. *Journal of Aircraft*, 55(3):1082–1089, 2018. doi: 10.2514/1.C034529.

[16] D. Kraft. A software package for sequential quadratic programming. Technical Report DFVLR-FB 88-28, Wiss. Berichtswesen d. DFVLR, 1988.

[17] G. Kenway, C. Mader, P. He, and J. Martins. Effective adjoint approaches for computational fluid dynamics. *Progress in Aerospace Sciences*, June 2019. doi: 10.1016/j.paerosci.2019.05.002.

[18] N. R. Secco, J. Jasa, G. K. Kenway, and J. R. R. A. Martins. Component-based geometry manipulation for aerodynamic shape optimization with overset meshes. In *18th AIAA/ISSMO Multidisciplinary Analysis and Optimization Conference*. American Institute of Aeronautics and Astronautics, Inc., 2017. doi: 10.2514/6.2017-3327.